



Morphology, Crystal Structure and Thermal Properties of Nano-Sized Amorphous Colemanite Synthesis

Sezai Kutuk¹

Received: 17 October 2023 / Accepted: 28 January 2024
© The Author(s) 2024

Abstract

It is important to utilize the raw colemanite (RC) mineral, which has abundant reserves in the world, and to reduce its particles to smaller sizes for nanotechnology. However, not only the particle size of the produced colemanite powder but also its other properties need to be elucidated. By using the Taguchi design, the RC mineral was ground in a high-energy ball mill. From signal-to-noise (S/N) ratio, the smallest average particle size was found to be $3.10\ \mu\text{m}$ for the experiment E04/nano-sized amorphous colemanite (NAC) powder. The characteristics of as-received RC mineral and synthesized NAC material were investigated using laser particle size analyzer, optical microscopes, SEM–EDS, XRD, TEM, HRTEM, and TGA–DTA devices. It was found that the NAC powder was not homogeneous, a small peak within the $300\text{--}20\ \text{nm}$ range appeared, and d_{90} , d_{50} , d_{10} , and d_{min} values were, respectively, $14.6\ \mu\text{m}$, $3.08\ \mu\text{m}$, $232\ \text{nm}$, and $26\ \text{nm}$. In the XRD analysis, the pure colemanite, calcite, and silica minerals were determined. The crystal structure of the NAC powder almost turned amorphous, and the crystallite size of (031) peak was reduced to $7.3\ \text{nm}$. It was deduced that the average particle size was $8.29\ \text{nm}$ ($R^2 = 0.86$), and the d -spacing value was $0.307\ \text{nm}$. This significant finding was attributed to the mobility of balls and moreover it was interpreted with an equation. An unknown transition in TGA–DTA was referred to the calcite mineral. Finally, it is believed that the synthesized NAC material will be beneficial to engineering studies as a natural/mineral additive.

Keywords Boron · Taguchi design · Ball milling · Amorphous · Crystallite size · Mineral additive

1 Introduction

Boron's insufficient electrons allow it to create compounds with metals and nonmetals. These compounds are in demand in engineering applications because of their exceptional technical qualities. Nevertheless, commercial minerals having boron oxygen bonding (B–O) such as colemanite, ulexite, and tincal (boron ores) include boron trioxide (B_2O_3) at different proportions. When it comes to B_2O_3 reserves under the earth's crust, Turkey has a large position with a reserve of 952 million tons or 73.2% of the total reserve. R&D operations in Turkey, which has the world boron market share of 57%, have been progressively rising in conjunction with resource development operations in the boron deposits. In this context, colemanite

($2\text{CaO}\cdot 3\text{B}_2\text{O}_3\cdot 5\text{H}_2\text{O}/\text{Ca}_2\text{B}_6\text{O}_{11}\cdot 5\text{H}_2\text{O}/\text{Ca}_2\text{B}_6\text{O}_8(\text{OH})_6\cdot 2\text{H}_2\text{O}$: Calcium-Borate Hydrate) is one of the major boron minerals that are extracted in largest quantities from mines as part of these operations. This mineral is utilized in its natural form, its compound/alloy form, or waste. As a result, the colemanite mineral has a wide range of areas that are already in use and will be in the future. The mineral has gained a reputation as a cutting-edge product in the fields of research, advanced engineering, and business. Glass, fiberglass, enamel, fertilizer, agrochemical, detergent, cosmetics, antiseptic, disinfectant, flame retardant, textile, adhesive, metallurgical slag, cement, permanent magnet, nuclear power plant [1, 2], asphalt concrete [3], road concrete [4], B_4C composite armor, hydrogen energy storage, and electric vehicle battery [5] can be given as a few examples.

Since the Nobel laureate physicist Richard P. Feynman introduced the term 'nanotechnology' in his well-known 1959 speech 'There's Plenty of Room at the Bottom: An Invitation to Enter a New Field of Physics,' many breakthrough technologies have occurred. Nanotechnology is the quantum effect that allows intervening in the matter at the

✉ Sezai Kutuk
sezai_kutuk@hotmail.com; sezai.kutuk@erdogan.edu.tr

¹ Department of Marine Engineering, Faculty of Turgut Kiran Maritime, Recep Tayyip Erdogan University, 53900 Derepazari, Rize, Turkey



atomic level. Nanoparticles (NPs), which attract attention with their extraordinary technical properties, are among the main constituents of nanotechnology. NPs are ultra-fine particles with a very high specific surface area (SSA). Based on the material and usage, their meanings can change. NPs are simply defined as particles whose physical characteristics of a solid-state material that is less than 100 nm in size are likely to be different [6]. NPs have better mechanical [7], thermal [8], electrical [9], magnetic [10], and other characteristics than micron particles. Accordingly, NPs are employed in industrial applications and also studied in-depth for new usages in a variety of fields today [11].

Chemical vapor deposition, sol-gel synthesis, high-energy ball milling (HEBM), and other techniques are utilized to decrease the particle size of a material to the nanometer scale. HEBM technique, which is a solid-state process, is favored owing to the fact that it has cheaper cost, shorter processing time, and more material types [12]. The main advantages of HEBM technique are smaller particle/crystallite/grain size, nanoparticle/nanocrystalline/nanostructure/nanosheet/nanopowder formation, amorphous structure transformation, alloy/compound/composite formation, lower annealing/calcination/sintering/melting/glass transition temperature, removal of undesirable components such as CO_2 and crystal H_2O , a uniform particle size distribution (PSD)/phase, narrower PSD/phase, bigger SSA, stronger the corrosion resistance/thermal resistance, greater hardness/strength, and faster the kinetics of hydrogen absorption/desorption. In addition, this technique involves the deformation, fracture, and welding mechanism (mechanical activation) of particles on a continuous basis. Particles are exposed to high energetic impact between the balls and the walls of the vial or between the balls. Because HEBM contains high kinetic energy compared to other ball milling techniques, milling parameters are of great importance. Milling time, ball-to-powder mass ratio (BPR), rotation speed, process control agent (PCA), ball size, vial size, filling degree of the vial, milling atmosphere, material type, and feed size are the essential factors for milling efficiency. Moreover, the nanoparticle grinding of industrial minerals and rocks such as limestone, sand, quartz, graphite, feldspars, gypsum, kaolinite, zeolites, and borates is a critical unit process. However, since the colemanite mineral is a ceramic material (generally brittle due to the difficulty of dislocation motion, or slide), its easy disintegration provides an advantage in terms of milling costs.

Waclawska [13] purified the raw coarse-crystalline colemanite mineral (no detail) before milling it from 1 to 90 h using a laboratory vibration mill. It was observed from scanning electron microscope (SEM) micrographs that particle size was reduced and particle shape became more irregular at a milling time of 1 h, that particles were agglomerated

at a milling time of 10 h, and that particle shape became almost spherical at a milling time of 24 h. Additionally, it was ascertained from X-ray diffractometer (XRD) patterns that the crystal structure of the colemanite mineral was slightly deformed at 24 h while the crystal structure nearly transformed into an amorphous phase at 90 h.

Kutuk-Sert [4] produced the concrete samples for road pavement with milled and sieved raw colemanite minerals (C – 75 μm : the undersize 75 μm colemanite, C – 45 μm , and C – 25 μm). C – 75 μm and C – 45 μm (40 wt% B_2O_3) powders were used as received. In the initial step of the research, C – 25 μm powder was prepared from as-received C – 3 mm mineral (36 min wt% B_2O_3) by the HEBM technique for 30 min. The particle size analysis of the colemanite powders was performed via a laser diffraction (LD) particle size analyzer. The C – 25 μm powder showed the best average particle size value (d_{50}) with 8.11 μm , and its particle shape was not exactly normally spherical but more spherical than unmilled. Likewise, the C – 25 μm powder again revealed the lowest particle size value (d_{min}) with 316 nm. As a result, the colemanite mineral's particle size was decreased to the submicron scale. Findings of the LD particle size measurement were verified by SEM micrographs. In the next step of the research, the colemanite powders were mixed into the concrete samples as a mineral additive at varying rates. The 28-day compressive strength of the concrete improved for all samples. The improvement observed especially in the C – 25 μm powder was based on the fact that the powder gave high adherence by filling the interface between the aggregate and cement paste.

Uysal et al. [14] first ground raw colemanite mineral (49.38 wt% B_2O_3) for very short time by using a porcelain ball mill and later passed it through sieves with – 212 + 53 μm fraction. After being held at 105 °C in the oven to get rid of moisture, the sieved powder was ground by the HEBM technique for up to 150 min. On the basis of SEM micrograph, the particle size of colemanite powder was around 10 μm for 45 min milling time and its particle shape was irregular. Besides, not only agglomeration (mostly) but also aggregation happened in the colemanite mineral. Furthermore, as can be seen from XRD patterns, the crystal structure of the colemanite mineral was deformed at 45 min and even turned amorphous at 150 min.

Kutuk and Kutuk-Sert [15] fabricated mixtures for asphalt pavement with milled and sieved raw colemanite minerals (C + 53 μm : the oversize 53 μm colemanite and C – 25 μm powders). In the first stage of the study, as-received C – 3 mm mineral (30.43 wt% B_2O_3) was milled using the HEBM technique for 30 min. Afterward, ground powder was screened through 53 μm and 25 μm meshes. The d_{50} and d_{min} values of the C – 25 μm powder were found to be 7.06 μm and 275 nm from LD particle size analyzer, in turn, whereas the particle shape of the C + 53 μm powder was spherical,

that of the C – 25 μm powder was not fully spherical. The existence of particles less than 100 nm in the C – 25 μm powder was roughly observed in the SEM micrograph. The discrepancy between LD particle size and SEM particle size was ascribed to the agglomeration of particles. In the final stage of the study, the colemanite powders were added to the asphalt mixtures as a mineral additive at different ratios. The Marshall stability, Marshall quotient, indirect tensile stiffness modulus, rutting resistance, and vertical deformation values of the asphalt mixtures were enhanced with the addition of colemanite. The fact that the vertical deformation value of the C – 25 μm powder was determined to be lower than that of the C + 53 μm powder was attributed to the particle size being on a nano/submicron scale.

The main objective of the present study is to decrease the particle size of the raw coarse boron mineral to smaller nano-size using Taguchi design via the HEBM technique and also to examine the microstructure, nanostructure, elemental composition, crystal structure, and thermal properties of the synthesized mineral powder in detail. In the literature, there is a very limited number of studies on nano-sized colemanite mineral. As a result of the present study, colemanite mineral powder with finer nanoparticles, smaller crystallite size, and an amorphous state has been successfully obtained by using Taguchi design, and its basic properties have been extensively investigated. Besides, XRD and TEM analyses performed in this study will be helpful in engineering studies (for example, reducing CO₂ emissions by saving cement and bitumen) using mineral additive powders, which need information on not only the nano-size but also the amorphous state.

2 Materials and Methods

2.1 Initial Material

Raw/natural colemanite mineral was supplied from the Eti Maden Operations Bigadic Boron Operations Directorate's mines. The colemanite mineral, sieved using a 3.35 mm mesh (No.6), was utilized as the initial material. Table 1 shows the chemical and physical characteristics of the raw colemanite (RC) mineral (coarse powder), and also more information is given in other studies [16, 17]. Figure 1 illustrates the flowchart for the experimental procedure.

2.2 Ball Milling Process

As-received RC mineral was mechanically milled in a planetary high-energy ball mill (Retsch, model 'PM 100') in the air environment in order to achieve a lower particle size/crystallite size. Zirconia vial and balls were preferred in order to elude contamination during milling process. The ball diameter of 5 mm, the vial volume of 250 ml, and

the methanol for process control agent (PCA) type (Merck, purity of 99.99%) were kept constant taking account of previous study results [15, 18, 19], but PCA amount, the rotational speed, ball-to-powder mass ratio (BPR), and milling time were changed. Table 2 presents factors and levels of the milling process. The mill was stopped every 15 min to minimize overheating and agglomeration, and after 5-min intervals, it proceeded to operate in the other direction.

2.3 Taguchi Design

The Taguchi design is a statistical method used to increase the functionality of applied science and engineering in an empirical study. Because of statistical variation, this method requires fewer experiments to analyze all input parameters and filters out a few effects. As a consequence, finding out the optimal experimental condition becomes simpler.

To find out the effect of milling process parameters on the average particle size of milled powders, an L₁₆(4⁴) orthogonal array design given in Table 3 was utilized for this study. A 'smaller is better' approach given in Eq. (1) based on the static problem was used to calculate the signal-to-noise (S/N) ratio [20]:

$$S/N = -10 \log \left[\frac{1}{n} \sum_{i=1}^n (y_i^2) \right] \quad (1)$$

where y_i and n denote the average particle size (d_{50}) and the number of iterations, respectively.

2.4 Measurements

The particle size distributions (PSDs) of the RC mineral and milled powders were analyzed by using an LD particle size analyzer (Malvern, model 'Mastersizer Hydro 2000 MU'). Powders were ultrasonically dispersed in water for 1 min. By scanning each powder four times, the analyzer calculated the average value. The cumulative volume percent passing as 90%, 50%, 10%, and the minimum was, respectively, marked as the d_{90} , d_{50} , d_{10} , and d_{\min} values.

Micron-size images of the RC mineral and milled powder were examined with a stereo optical microscope (SOM; Olympus, model 'SZ61') including a digital camera capable of $\times 5$ optical magnification (Samsung, model 'ES73'). The scaling of the image was performed by means of millimeter paper. In addition, their micron-size images were investigated by a polarizing optical microscope (POM; Olympus, model 'BX51') including both a camera (Olympus, model 'DP72') and the Stream Basic software.

Micrographs of the RC mineral and milled powder were taken with an SEM (Jeol, model 'JSM-6610') at an accelerating voltage of 20 kV as soon as the powders were coated

Table 1 Chemical and physical properties of the raw colemanite mineral

Chemical properties		Physical properties	
Component	Raw colemanite (wt%)		
B ₂ O ₃	36 min	Mohs hardness	4–4.5
CaO	30 max	Specific weight	2.42 g/cm ³
SiO ₂	5 max	Dissolution	Slowly in water
SO ₄	0.45 max	Dissolution	Rapidly in HCl
As	40 ppm max	Transparency	Transparent
H ₂ O [Lotti]	21.8	Crystal system	Monoclinic
MgO, SrO, Al ₂ O ₃ , Na ₂ O, Fe ₂ O ₃ [Kutuk-Sert]	5.33 max	Particle size	Undersize 3 mm
Moisture	1 max		
Total	~ 99.58		

Fig. 1 Flowchart for the experimental method

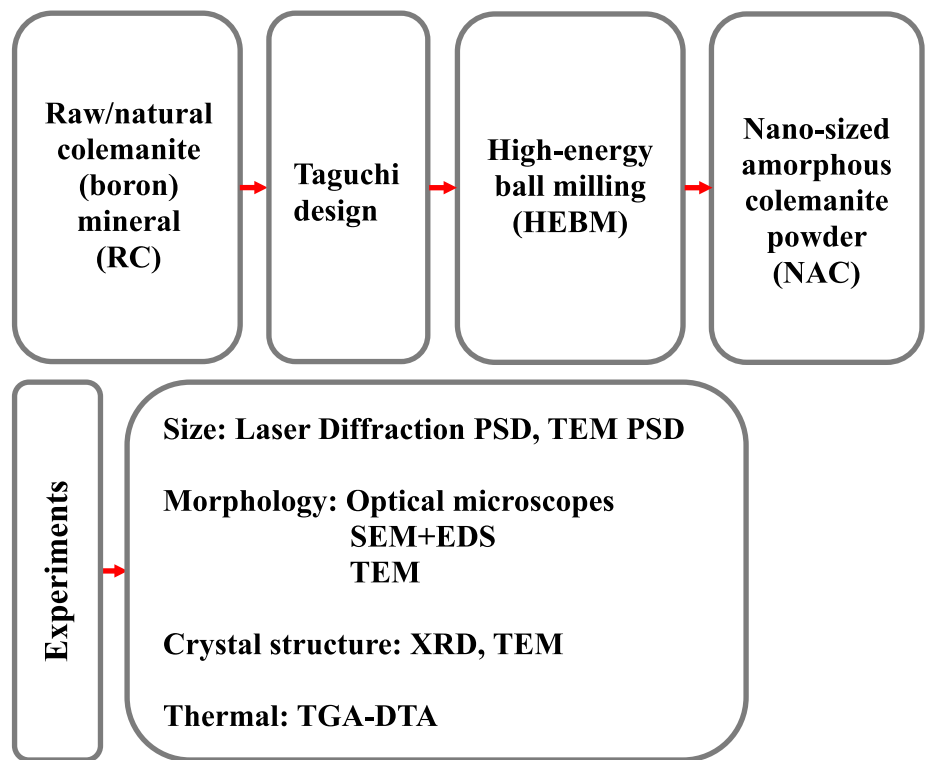


Table 2 Factors and levels of the milling process

Levels	Factors			
	A	B	C	D
	PCA (wt%)	Speed (rpm)	BPR	Time (min)
1	0	200	2:1	15
2	2	400	5:1	30
3	5	500	10:1	60
4	10	600	20:1	120

Table 3 Taguchi's $L_{16}(4^4)$ orthogonal array and responses of average particle size/ d_{50} and S/N ratio

Experiments	A	B	C	D	y_i (μm) (particle size)	S/N ratio
E01	1	1	1	1	2863.1	-69.137
E02	1	2	2	2	2701.4	-68.632
E03	1	3	3	3	20.5	-26.218
E04	1	4	4	4	3.1	-9.757
E05	2	1	2	3	602.4	-55.598
E06	2	2	1	4	713.1	-57.064
E07	2	3	4	1	26.7	-28.525
E08	2	4	3	2	11.9	-21.540
E09	3	1	3	4	1000.0	-60.000
E10	3	2	4	3	12.4	-21.864
E11	3	3	1	2	609.0	-55.693
E12	3	4	2	1	345.2	-50.761
E13	4	1	4	2	3000.0	-69.542
E14	4	2	3	1	2718.9	-68.688
E15	4	3	2	4	61.8	-35.825
E16	4	4	1	3	107.9	-40.659

with gold for conductivity. Particle sizes were estimated from the SEM micrograph using the ImageJ 1.53a (NIH) software and graphing software. Their elemental compositions were quantified via an energy dispersive X-ray spectrometer (EDS; Oxford Inst., model 'x-act') integrated with the SEM. The quantitative values were obtained from the mapping analysis in the selected area. The dead time was adjusted for the element boron.

Crystal structures of the RC mineral and milled powder were carried out an analysis by an XRD (Rigaku, model 'SmartLab') with $\text{CuK}\alpha$ source ($\lambda = 1.541 \text{ \AA}$). XRD patterns were collected in the 2θ range of 4° – 60° in a step size of 0.02° . Quantitative analysis was fulfilled with the PDXL software. The average crystallite size (D) was estimated from the Scherrer equation in Eq. (2)[21]:

$$D = \frac{K\lambda}{\beta \cos \theta} \quad (2)$$

where β , θ , and K symbolize successively the full width at half maximum intensity (FWHM) in rad, the Bragg's diffraction angle, and the shape factor (0.9).

To characterize the nanoparticle size and crystalline nature of the RC mineral and milled powder, a high-resolution transmission electron microscopy (HRTEM; FEI, model 'Tecnai G2 F30') was employed under an accelerating voltage of 200 kV. Particle sizes, lattice fringes, and crystallite sizes were calculated from the TEM micrograph using the ImageJ 1.53a (NIH) software and graphing software.

Thermogravimetry–differential thermal analysis (TGA–DTA) tests of the RC mineral and milled powder were made by means of a simultaneous thermal analyzer

(Netsch, model 'STA 449 F3 Jupiter'). These analyses had the TS EN ISO/IEC 17025 standard and the EU 0403-T accreditation certificate. Moreover, all tests were conducted in the temperature range of 25–1000 °C temperature, heating rate of 10 °C/min, and flowing nitrogen atmosphere.

3 Results and Discussion

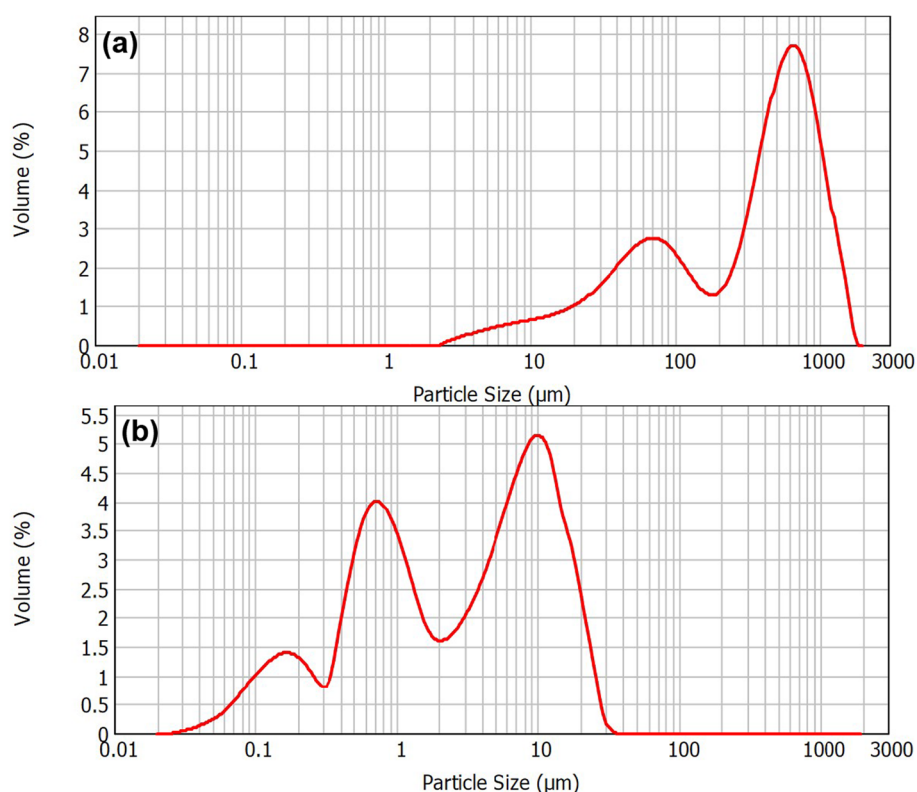
3.1 Laser Diffraction PSD Analysis

The RC mineral was subjected to a milling process using the Taguchi design and the average particle size/ d_{50} values of the 16 powders obtained are listed in Table 3. The lowest d_{50} value was found to be 3.10 μm for the experiment E04/nano-sized amorphous colemanite (NAC) powder. In the course of this study, the RC mineral and the NAC powder will be scrutinized from this point with the aim of focusing on smaller nanoparticles/nanocrystallite size.

Figure 2a, b shows the differential volume PSDs of the RC mineral and the NAC powder, respectively. While the RC mineral has a bimodal PSD with a large peak in the 2000–200- μm interval, and a small peak in the 200–2- μm interval, the NAC powder has a trimodal PSD with a large peak in the 40–2- μm interval, a moderate peak in the 2–300-nm interval, and a small peak in the 300–20-nm interval. This finding indicates that particle size was significantly reduced with the milling process although there is non-uniform distribution. In the study conducted by Kutuk & Kutuk-Sert [15], the milled raw colemanite mineral ($C - 25 \mu\text{m}$) was found to have a bimodal PSD with a large peak in the 40–2- μm



Fig. 2 Particle size distributions of **a** as-received raw colemanite (boron) mineral and **b** nano-sized amorphous colemanite powder



interval and a small peak in the 2–200-nm interval, but in the present study, another nanoscale peak was observed. The present study and the study reported by Guzzo et. al [22] are similar, with the latter reporting that nanoparticles could be successfully obtained by milling the raw Tanhaçu quartz mineral using the HEBM technique, although the heterogeneity of PSD increased.

The d_{90} , d_{50} , d_{10} , and d_{\min} values of the RC mineral are 995 μm, 410 μm, 29.0 μm, and 2.51 μm, in turn. Nevertheless, the d_{90} , d_{50} , d_{10} , and d_{\min} values of the NAC powder are 14.6 μm, 3.08 μm, 232 nm, and 26 nm, respectively. Thanks to the milling process, a number of notable findings were reached as follows: (i) The distribution range ($\Delta H = d_{90} - d_{10}$) value drastically decreased from 965 μm to 14.4 μm, meaning that PSD shrunk; (ii) the d_{50} value sharply diminished from 410 μm to 3.08 μm; therefore, very fine powder could be obtained; (iii) the d_{10} value dropped from 29.0 μm to 232 nm, meaning that submicron particles were found; (iv) The d_{\min} value severely decreased from 2.51 μm to 26 nm; thus, the nanoparticle could be achieved.

The d -values of the NAC powder are quite good compared to the d -values ($d_{90} = 18.8$ μm, $d_{50} = 7.06$ μm, $d_{10} = 636$ nm, and $d_{\min} = 275$ nm) of the C – 25 μm in another study [15]. Furthermore, it is remarkable that the average/median particle size was reduced to 3.08 μm with a decrease of 43.5% and, as can be seen in Fig. 2b, the presence

of particles below < 100 nm was detected. These considerable findings can be explained by the compressive force and shearing force exerted by the balls on the NAC powder. The greater the compressive force and shearing force of the powder particle is repetitively exposed to, the more the threshold energy required for particle breakage is reached. Therefore, it is comprehended that the milling parameters selected for the acquirement of the NAC powder are suitable for obtaining a smaller average particle size and nanoparticles.

The specific surface area (SSA) value is 0.04 m²/g for the RC mineral and 3.65 m²/g for the NAC powder. In other words, it was realized that the SSA value increased with the HEBM technique. The SSA value of NAC powder is much higher than the 1.12 m²/g value of C – 25 μm powder in the previous study [4]. It was emphasized that [23] bigger SSA values for a fine powder may give rise to stronger surface resistance, and smaller particles may cause large amounts of Van der Waals forces of attraction (adhesion). Finally, it is believed that the use of milled colemanite mineral as an admixture material will stand out in various engineering applications due to both its high SSA value and low d -values.

3.2 Optical Microscope Analysis

Figure 3a displays the SOM image of the RC mineral under $\times 6$ magnification. The RC mineral possesses various color tones including white, black, brown, and colorless. It is

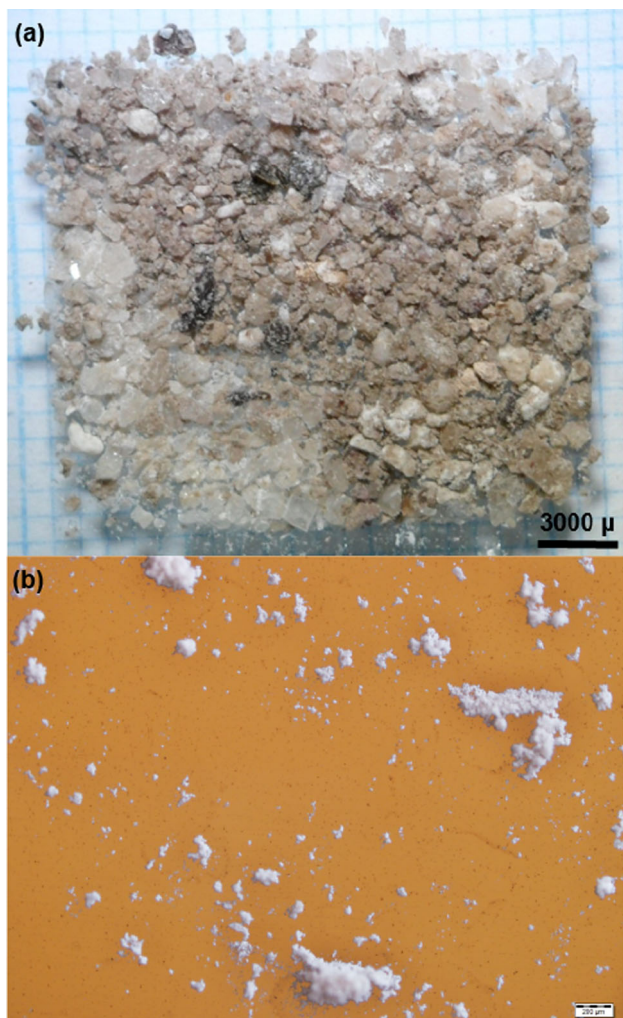


Fig. 3 Optical microscope images of **a** raw colemanite mineral for $\times 6$ SOM and **b** nano-sized amorphous colemanite powder for $\times 40$ POM (white color denotes the milled powder, and orange color indicates the substrate)

known that [24] the color of raw colemanite mineral is colorless/white and its other colors originate in impurities/crystal shape. When the data in Table 1 are examined, the following can be inferred: The percentage of B_2O_3 , CaO, and H_2O , the components of pure colemanite mineral, by weight corresponds to ~ 88 and the percentage of the components of other impurity minerals (SiO_2 , MgO, SrO, SO_4 , Al_2O_3 , Na_2O , Fe_2O_3) is by weight equivalent to ~ 11 . However, raw colemanite mineral additionally comprises impurity minerals such as calcite ($CaCO_3$), cristobalite (SiO_2), dolomite ($CaMg(CO_3)_2$), celestite ($SrSO_4$), and clay. On account of the CaO components originating from other impurities, the 30 max wt% CaO value given in Table 1 equals the sum of not only component of the pure colemanite mineral but components of impurity minerals. For the 36 wt% B_2O_3 value in

the present study, the RC mineral was calculated to have 71 wt% purity from mass percent composition.

The particles have big sizes, various shapes, clear edges, and corners. Besides, particle size mainly ranges from 1500 to 500 μm (coarse powder). This observation is in line with the $d_{90} = 995 \mu m$ and $d_{50} = 410 \mu m$ values of LD PSD in Fig. 2a.

Figure 3b represents the POM image of the NAC powder under $\times 40$ magnification. The milled powder is white, slightly agglomerated, and has a particle size below 50 μm (very fine powder). The reason why the uniformly distributed powder obtained through a milling process at submicron or nano-size is perceived white is that all wavelengths of the visible light spectrum reach the eye at the same time. It was ascertained that the NAC powder had more homogeneous distribution than the RC mineral. Furthermore, it was decided that particle size was significantly reduced at the end of the milling process, and the powder turned into a single color.

3.3 SEM-EDS Analysis

Figure 4a shows the SEM micrograph and histogram of the RC mineral under $\times 30$ magnification. It was observed that the particles generally had big sizes, irregular shapes, and a rough face, while some particles had an angular shape. The smallest particle size is 11 μm and the largest one is 1369 μm . This means that PSD is very broad and has a good fit with the LD PSD measured at the 2–2000- μm interval in Fig. 2a. The average particle size was calculated as 319 μm using a three-parameter Gaussian fit curve from the histogram ($R^2 = 0.76$). When the width of PSD is taken into consideration, this value is close to the measured $d_{50} = 410 \mu m$.

Figure 4b–d displays the SEM micrographs and histograms for the detailed analysis of the NAC powder under $\times 1 k$, $\times 5 k$, and $\times 15 k$ magnification. First, it was determined from $\times 1 k$ that the particle size ranged from 301 nm to 26 μm and was substantially below 10 μm . This finding suggests that PSD considerably narrowed with the milling process and, moreover, it is in accordance with both two of the trimodal peaks in Fig. 2b (the peak in the 40–2- μm interval and the peak in the 2 μm –300-nm interval) and POM results. In comparison with the SEM micrograph of the C – 25 μm powder under $\times 1 k$ magnification published by Kutuk & Kutuk-Sert [15], the particle size in the present study is finer on average.

Secondly, it was seen from $\times 5 k$ that the particle shape was irregular, yet it is relatively more rounded than the unmilled mineral. The smallest particle size is 54 nm and the largest one is 4.48 μm . The average particle size was estimated as 448 nm based on the histogram ($R^2 = 0.96$). It was observed that the particles were agglomerated (not embedded or strong interfacial bonding), particularly around the large particle. This situation can be attributed to the fact that agglomeration

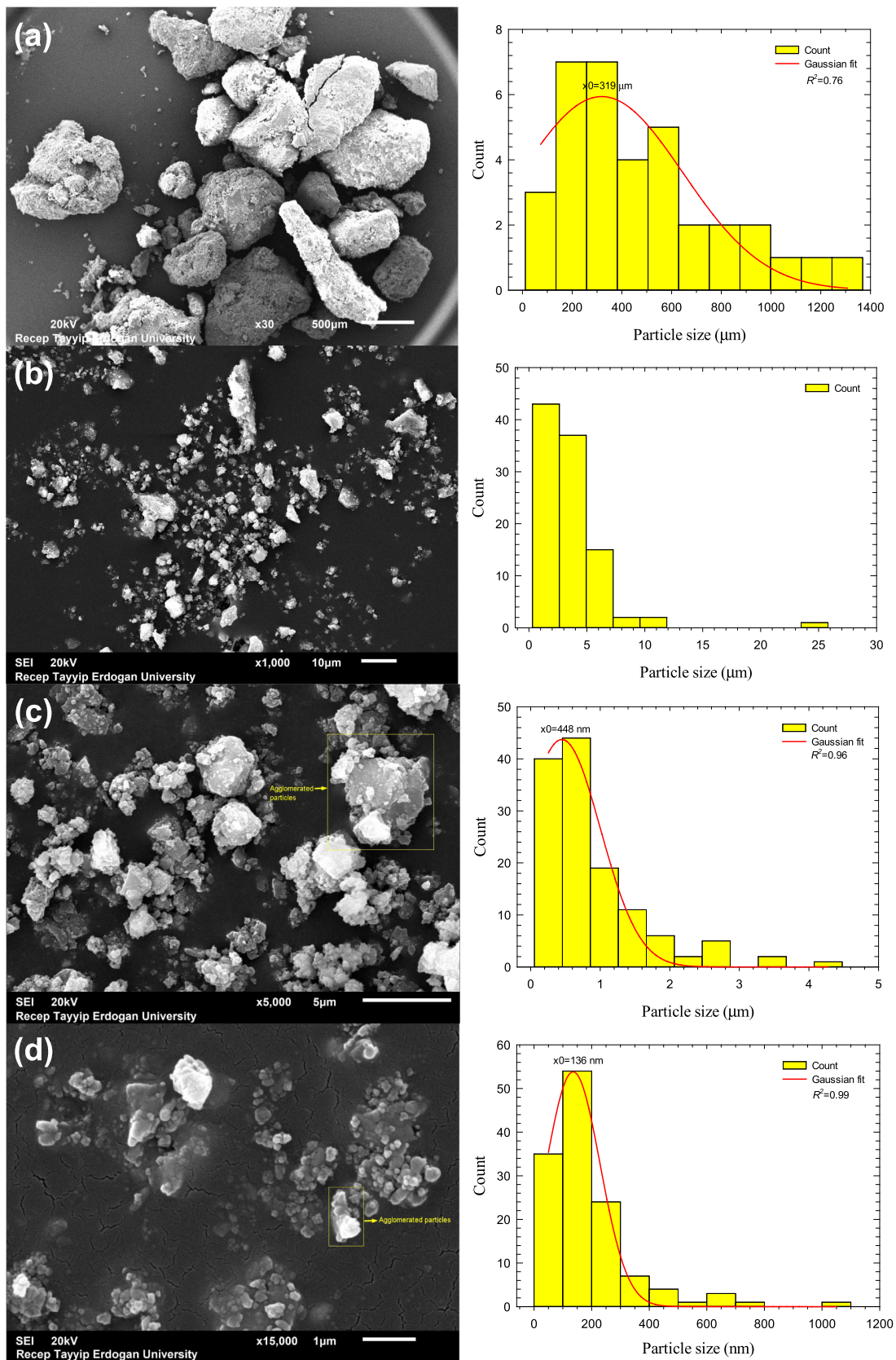


Fig. 4 SEM micrographs and histograms of **a** raw colemanite mineral under $\times 30$, and of nano-sized amorphous colemanite powder under **b** $\times 1 \text{ k}$, **c** $\times 5 \text{ k}$, **d** $\times 15 \text{ k}$

stems from van der Waals forces, which have weak bond structure between the particles [25].

Thirdly, it was detected from $\times 15$ k that the smallest particle size was 34 nm and the largest one was 1.04 μm . This finding points out that PSD shrunk with the milling process, and also it is compatible with the other trimodal peak in Fig. 2b (the peak in the 300–20-nm interval). The average particle size was calculated as 136 nm based on the histogram ($R^2 = 0.99$). It was determined that the Gaussian fit curve overlapped with very good experimental data. Agglomerated particles were observed, and it was noticed that particles with smaller size were more rounded in shape. Although it was stated in earlier studies that particles were agglomerated as a result of the reduction of boron mineral particles to submicron/nano-size thanks to the milling process carried out using a ball mill [15, 18, 19], particle agglomeration is more clearly observed in the present study.

The reason for slightly larger particle size in the LD PSD measurement (Fig. 2) could be ascribed to the difficulty encountered in the distribution of the particles during the experiment. Such an event has been confronted in other similar studies [15, 26]. In sum, it was concluded from these three different magnification data that particle size was dramatically dropped at the end of the milling process, PSD shrunk, agglomeration happened, and the existence of nanoparticles was described.

Figure 5a demonstrates the EDS spectrum and quantitative elemental analysis of the RC mineral. The total weight percentage of the elements O, Ca, and B in the RC mineral was detected as 94.4%, which implies colemanite's chemical components of $2\text{CaO}\cdot 3\text{B}_2\text{O}_3\cdot 5\text{H}_2\text{O}$. However, the total weight percentage of the elements Si, Mg, Sr, Al, S and Na was determined as 5.5%, which reveals that the RC mineral involves impurities. This inference verifies the deductions made for the SOM analysis in Fig. 3a and is similar to the results of a previous study [15].

Figure 5b depicts the EDS spectrum and quantitative elemental analysis of the NAC powder. In the NAC powder, the total weight percentage of the elements O, Ca, and B was identified as 89.2%, whereas the total weight percentage of the elements Si, Mg, Zr, Sr, Al, S, and Fe was discovered as 10.9%. After the milling, it was understood that not only a slight decrease happened in the total of the pure colemanite components (5.2%), but also that the NAC powder was contaminated with 2.3% Zr by weight from the vial and the balls during the milling process. Saghir et. al [27] declared that the intensity of the Zr peak in the EDS spectrum raised a lot with the prolongation of milling time from 4 to 32 h for alumina powder. Accordingly, Zr contamination by weight ascended from 9.9 to 33.2%. On the contrary, in another study [15], it was expressed that Zr contamination did not occur subsequent to the milling process. The major reason why such different conclusions emerge is milling parameters. Since the

milling parameters for the NAC powder in the present study were selected as 0% PCA, 600 rpm speed, 20:1 BPR, and 120 min time (see Table 2 and 3) the mobility of balls was much higher. Meanwhile, the fact that the outside temperature of the vial was found to be high (98 °C) at the end of the milling process confirms higher mobility. In brief, in view of the slight wear that arose from the vial and the balls, contamination happened in the NAC powder. Yet, it is also known that low amounts of zirconia contamination improve the mechanical properties of certain materials [27].

3.4 XRD Analysis

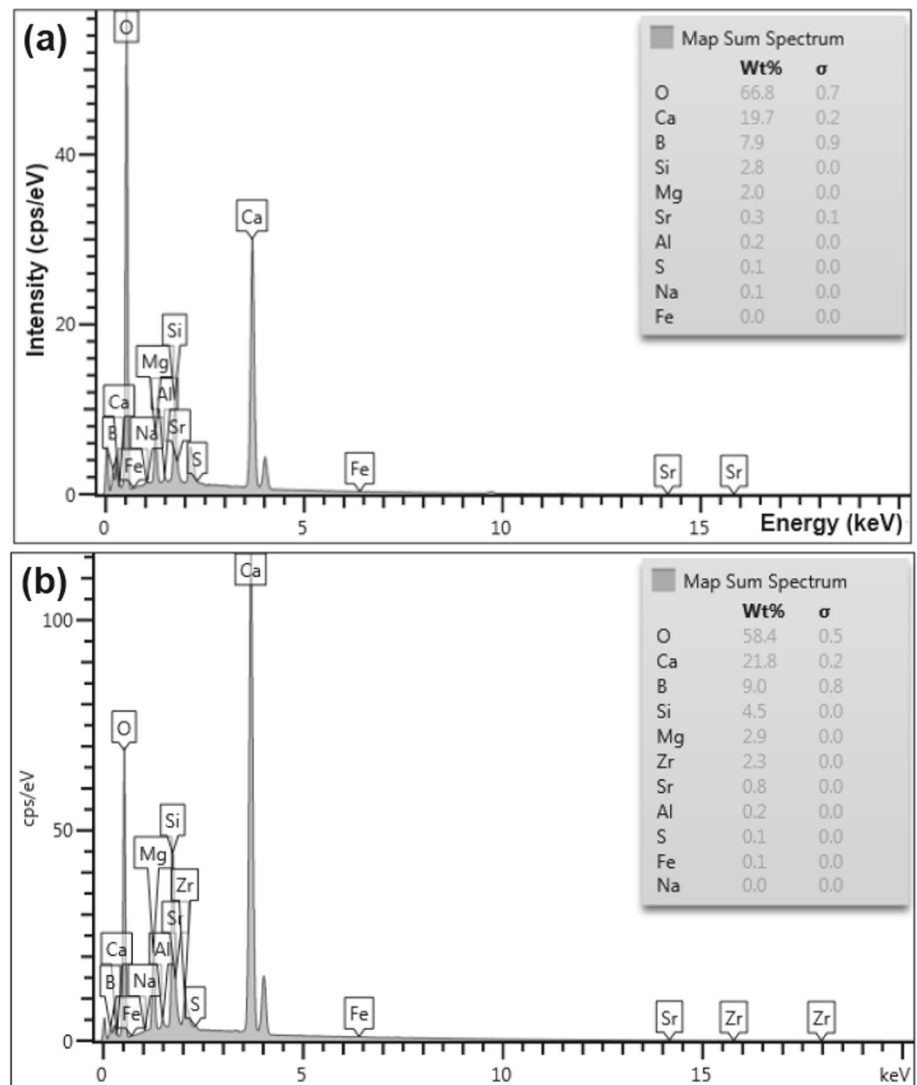
Figure 6a shows the XRD patterns of the RC mineral. The sharp peaks prove the high crystallinity of the RC mineral. The peak with the highest intensity is $I = 49,752$ (cps) for $2\theta = 15.84^\circ$ and coincides with the plane (020) on the colemanite file with PDF card no. 00–033–0267 (monoclinic, space group: $P2_1/a$, $d_{\text{meas}} = 2.42$ g/cm^3). This indicates that the major phase is the colemanite mineral, and it is in agreement with the raw colemanite mineral with 83 wt% purity in a previous study [28].

Apart from the pure colemanite mineral, the presence of CaCO_3 , SiO_2 , and other impurity minerals was discovered. Kutuk [16] said that the peak of the milled colemanite mineral (raw, – 3 mm) with the biggest intensity at $2\theta = 15.8^\circ$ was that of the pure colemanite mineral, and that the peak at $2\theta = 29.5^\circ$ was that of the impurity mineral. In the present study, the peak with $I = 16,466$ (cps) for $2\theta = 29.54^\circ$ overlaps with the distinctive plane (104) on the CaCO_3 (calcite) file with PDF card no. 01–085–0849. Yildiz [28] stated that the calcine colemanite mineral at 600 °C (– 250 μm , B_2O_3 : 42 wt%) dissolved into B_2O_3 and CaO amorphous forms and that components such as CaCO_3 and SrSO_4 did not decompose and the peak with the highest intensity at $2\theta \approx 29.5^\circ$ belonged to the CaCO_3 . These findings support the inference made in the optical microscope analysis section.

The peak with $I = 9728$ (cps) for $2\theta = 13.76^\circ$ intersects with the plane (211) on the SiO_2 (hypothetical silica) file with PDF card no. 01–073–3412. The minor SiO_2 (211) peak here verifies both the 5 max wt% SiO_2 value listed in Table 1 and the 2.8 wt% Si value shown in Fig. 5a.

Figure 6b displays the XRD pattern of the NAC powder. It is obvious that the crystal structure turned into a predominantly amorphous state in consequence of the milling process. The peak of the pure colemanite mineral with the biggest intensity (020) disappeared completely. However, as can be observed from the inset of Fig. 6b, the intensity of the peak with the highest intensity based on its PDF card at $2\theta = 28.45^\circ$ (031) decreased from 2527 (cps) to 735 (cps) for the NAC powder and the peak width also increased. At the end of the milling process, the crystallite size of peak (031) calculated from Eq. (2) diminished from 228 nm to 7.3 nm.

Fig. 5 EDS spectra and quantitative elemental analyses of **a** raw colemanite mineral and **b** nano-sized amorphous colemanite powder



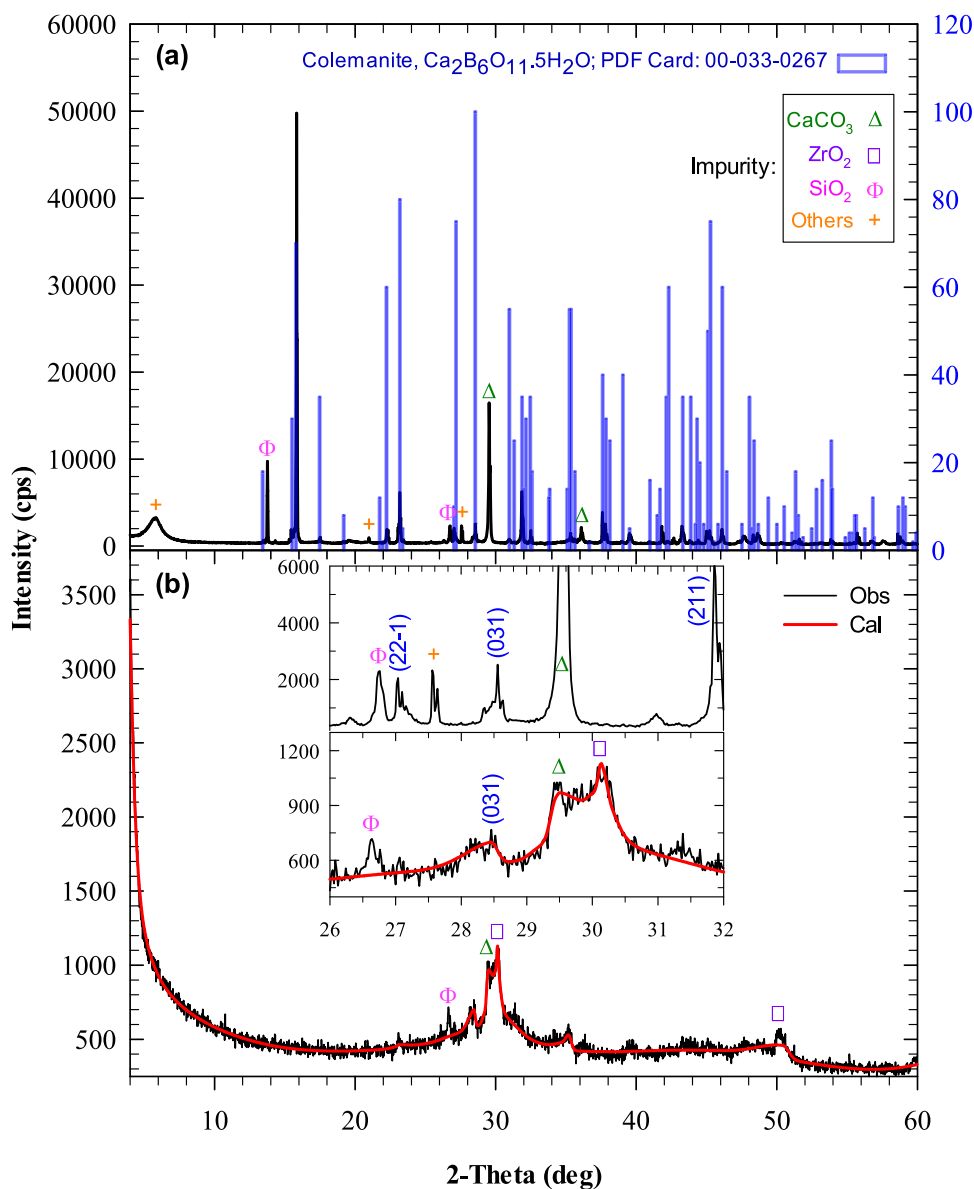
Namely, crystallite size for the raw colemanite mineral was successfully reduced to the nano-size. In comparison with the average crystallite size calculated as 63.6 nm in an earlier study [16], this value is quite low. This difference could most likely be ascribed to the fact that the kinetic energy transferred to the powder by the balls with high mobility was high due to the milling parameters used in the present study. It is emphasized that reducing crystallite size by means of the HEBM technique enhances the microhardness of the powder [29]. Thus, it is thought that the NAC powder will be plausible for mineral additives utilized to strengthen the mechanical properties of materials.

Waclawska [13] successfully turned the raw colemanite mineral into an amorphous state using the vibratory mill technique at 90 h, followed by Uysal [14] using the HEBM technique at 150 min, and the present study using the HEBM technique at 120 min. This result is remarkable for the commercial process due to the fact that the total energy transferred

from the balls to the NAC powder ($E_{p,t}$) reached a sufficient value in a shorter time thanks to the use of more suitable milling parameters.

Impurity peaks with very little intensity were encountered. An extra peak with $I = 1113$ (cps) at $2\theta = 30.22^\circ$ was identified, and this high-intensity peak overlaps with distinctive plain (011) on the ZrO_2 (zirconia) file with PDF card no. 00-050-1089. This finding is consistent with Saghir et. al [27]'s finding: the ZrO_2 peak emerged in the XRD pattern as a result of milling alumina powder in HEBM. Furthermore, this finding also confirms the interpretation of 2.3 wt% Zr contamination detected in the EDS analysis. In the NAC powder, the intensity of peak (104) of calcite was extremely declined (see the inset of Fig. 6b) and its crystallite size diminished from 134 to 7.4 nm. The peak with $I = 717$ (cps) for $2\theta = 26.64^\circ$ intersects with distinctive plain (101) on the SiO_2 (quartz silica) file with PDF card no. 01-078-1252. The SiO_2

Fig. 6 XRD patterns of **a** raw colemanite mineral and **b** nano-sized amorphous colemanite powder (inset: zoom-in of $2\theta = 26\text{--}32^\circ$)



(101) peak verifies both the 5 max wt% SiO₂ value given in Table 1 and the 4.5 wt% Si value depicted in Fig. 5b.

Following the milling process, it was determined that peak positions slightly shifted towards small angles. This behavior was formerly observed for the aluminum/15 wt% hexagonal boron nitride composite powder obtained by the HEBM technique and refer to an increase in the residual stress and lattice strain [30].

It was decided that the crystallite size of the raw colemanite mineral was reduced to below 10 nm, that the crystal structure became nearly amorphous, and a small amount of zirconia contamination was formed.

3.5 TEM Analysis

Figure 7a shows the low-magnification TEM micrograph and histogram for the NAC powder. It was ascertained that the particle shape was partially irregular and moderately rounded. It was observed that the particles were agglomerated, which approves the SEM micrograph. Particle size was found out to be the minimum of 9 nm and the maximum of 318 nm, and largely < 100 nm. In other words, PSD did not exhibit a homogeneous distribution. Among the trimodal peaks in the LD PSD measurement demonstrated in Fig. 2b, these findings are in line with only the small peak in the 300–20-nm interval. The difference between these two measurements could possibly be due to two situations: (i) The

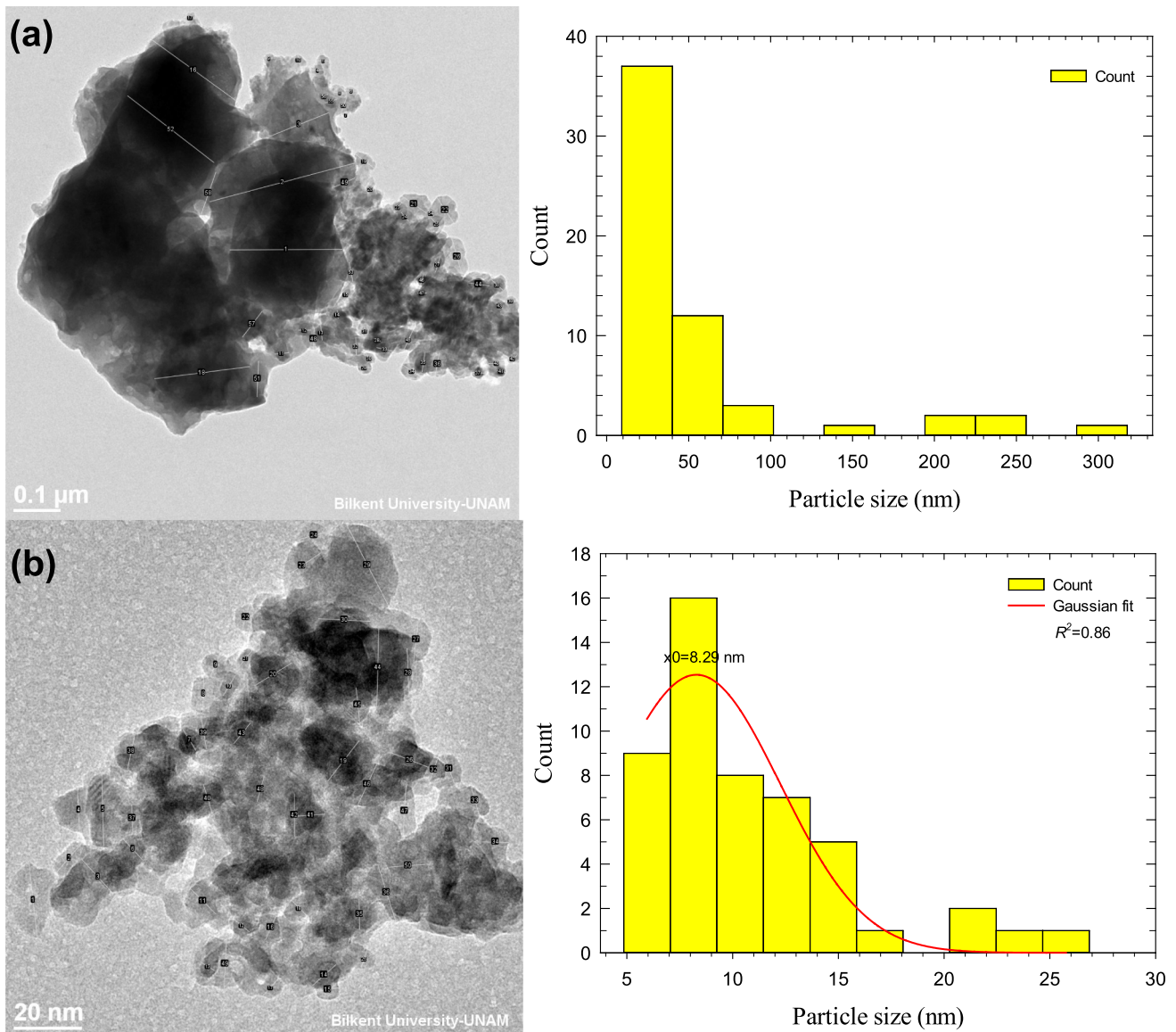


Fig. 7 **a** Low-magnification and **b** high-magnification TEM micrographs and histograms of nano-sized amorphous colemanite powder

agglomeration of the particles observed in the SEM micrograph and interpreted, (ii) the powder having a non-uniform distribution. Since dispensing the agglomeration in the powder used in the LD PSD is difficult for certain materials [26] and the milled powder has a high degree of heterogeneity [22], the measured size is actually the agglomeration particle size.

Figure 7b represents the high-magnification TEM micrograph and histogram of the NAC powder with the aim of distinguishing nanoparticles more clearly. It was observed that the particles were agglomerated, and the particle shape was well-rounded. The particle size was found to be 5 nm at the minimum and 27 nm at the maximum. It was realized that PSD exhibited an approximately homogeneous distribution. The Gaussian curve drawn in the histogram is congruent with

the $R^2 = 0.86$ and the average particle size is 8.29 nm. It can definitely be expressed that the particle size of the raw colemanite mineral was successfully reduced to the nanoscale. This achievement can be elucidated by the mobility of the balls. Based on Eq. (3), if the filling degree of the vial (φ) decreases, the circular radius (r_b) and velocity of the ball (v_b) increase. Hence, the kinetic energy of the ball heightens (K_b), which provides a positive effect [31, 32]. That is, in the present study, it was deduced that the particle size was reduced to the nanoscale as $E_{p,t}$ was bigger.

$$\begin{aligned} \varphi &= \frac{N_b V_b + V_p}{V_t}; K_b = \frac{(ka)}{2} m_b v_b^2 \\ &= \frac{(ka)}{2} m_b (\omega_b r_b)^2; E_{p,t} = P_{t} = N_b K_b \end{aligned} \quad (3)$$

where N_b , V_b , V_p , V_t , ka , m_b , ω_b , P_t , and t symbolize successively the number of the balls, the volume of a ball, the volume of powder, the volume of the vial, the powder ability, the mass of a ball, the angular velocity of a ball, the total power transferred to the powder, and milling time.

Figure 8a displays the HRTEM micrograph of the NAC powder. Crystal fringes can be obviously observed for different lattice planes of both the amorphous (irregular arrangement) structure and the crystal structure. The amorphous state observed here verifies the XRD result in Fig. 6b. Besides, inverse fast Fourier transform (FFT) (Fig. 8b) was applied to one of these fringes (rectangle yellow box in Fig. 8a). Figure 8c depicts that plot profile of the inverse FFT is smooth and has a d -spacing value of 0.307 nm. In the XRD analysis, this value has a good fit with the d -spacing value 3.135 Å of peak (031) in the colemanite file with PDF card no. 00-033-0267 at a rate of 98%. Moreover, as can be seen in Fig. 8a, the crystallite sizes of the NAC powder range between 2 and 20 nm. This range complies with the crystallite size of 7.3 nm for peak (031) calculated in the XRD analysis.

For example, it is known that the amorphous silica mineral, which acquired finer particle size ($d_{50} = 3 \mu\text{m}$), larger SSA value, and better chemical activity thanks to the milling process, improves compressive strength, flexural strength, and water resistance [33]. Therefore, it is hoped with the present study that the colemanite mineral with nanoparticles, much smaller crystallite size, and almost amorphous state will provide more advantages in various application fields.

3.6 Thermal Analysis

Considering that boron is consumed in the glass industry at a rate of 48% (global estimate for 2019) (borosilicate glass 22%, glass wool 15%, fiberglass 8%, TFT-LCD 3%) and in the ceramics industry at a rate of 15% [5], having knowledge of the thermal properties of the colemanite mineral exhibiting a glass-forming character, such as lower melting point, lower thermal expansion, and stronger thermal resistance, is of importance.

Figure 9a shows the TGA–DTA curves for the RC mineral. The TG (mass %) value of the RC mineral decreased to 99% at 325 °C, 95% at 400 °C, 88% at 500 °C, 87% at 625 °C, and 71% at 900 °C. It is obvious that mass loss in the RC mineral took place throughout two steps within the 325–500 °C and 625–900 °C intervals. In the DTG (mass loss rate) curve, a very sharp endothermic peak with maximum intensity was found at 397 °C and a broad endothermic peak was observed

at 835 °C. In the DTA curve, endothermic twin peaks with maximum intensity were determined at 388 °C and 401 °C as well as an endothermic peak at 835 °C, which is in agreement with the DTG curve. The behavior in the first step, or the twin peaks at 388 °C and 401 °C are the characteristic peak values of colemanite and indicate decomposition reaction. In clearer terms, it is the breaking of OH bonds from the crystal structure (pure colemanite: $2\text{CaO}\cdot 3\text{B}_2\text{O}_3\cdot 5\text{H}_2\text{O}$) (dehydroxylation) and the removal of a certain mole value (n) of H_2O crystal water (dehydration) from the structure (dehydrated colemanite) [13]. The behavior in the second step is an unusual situation because no severe loss occurs for the high-purity colemanite mineral in the TG curve within the 600–1000 °C interval, and this interval corresponds to the glass transition temperature (T_g), crystallization temperature (T_c), and melting temperature (T_m), in turn [34]. However, as given by Eq. (4), it is believed that the sharp transition in the 700–900 °C interval arose from the dissolution of the calcite mineral in the present study. This interpretation was made in reference to the TG analysis (– 50 μm calcite mineral sharply releases CO_2 with a value of ~ 40 wt% in the 700–900 °C interval) in another study [35] conducted for the raw calcite mineral/main CaCO_3 composition in limestone and the XRD analysis for the calcite mineral in this study.



Figure 9b displays the TGA–DTA curves for the NAC powder. The TG value of the NAC powder diminished to 97% at 325 °C, 96% at 400 °C, 94% at 500 °C, 92% at 625 °C, and 82% at 900 °C. It was understood that the mass loss for the NAC powder occurred throughout a single step rather than two steps within the 625–900 °C interval, therefore being different than that of the RC mineral. The fact that the twin peaks wholly disappeared is attributed to the deformation of the crystal structure of the colemanite mineral by virtue of the mechanical milling process and, consequently, its dehydration [13]. The near-amorphous state of the RC mineral in Fig. 6b evidences the deformation of the crystal structure. This finding gained with the HEBM technique is similar to the amorphous state of the colemanite mineral calcined at 600 °C by Yildiz [28]. In the light of this information, as given by Eq. (5), it was concluded that approximately 5 mol of crystal water moved away from the structure in the RC mineral at 600 °C and that the structure was amorphous.

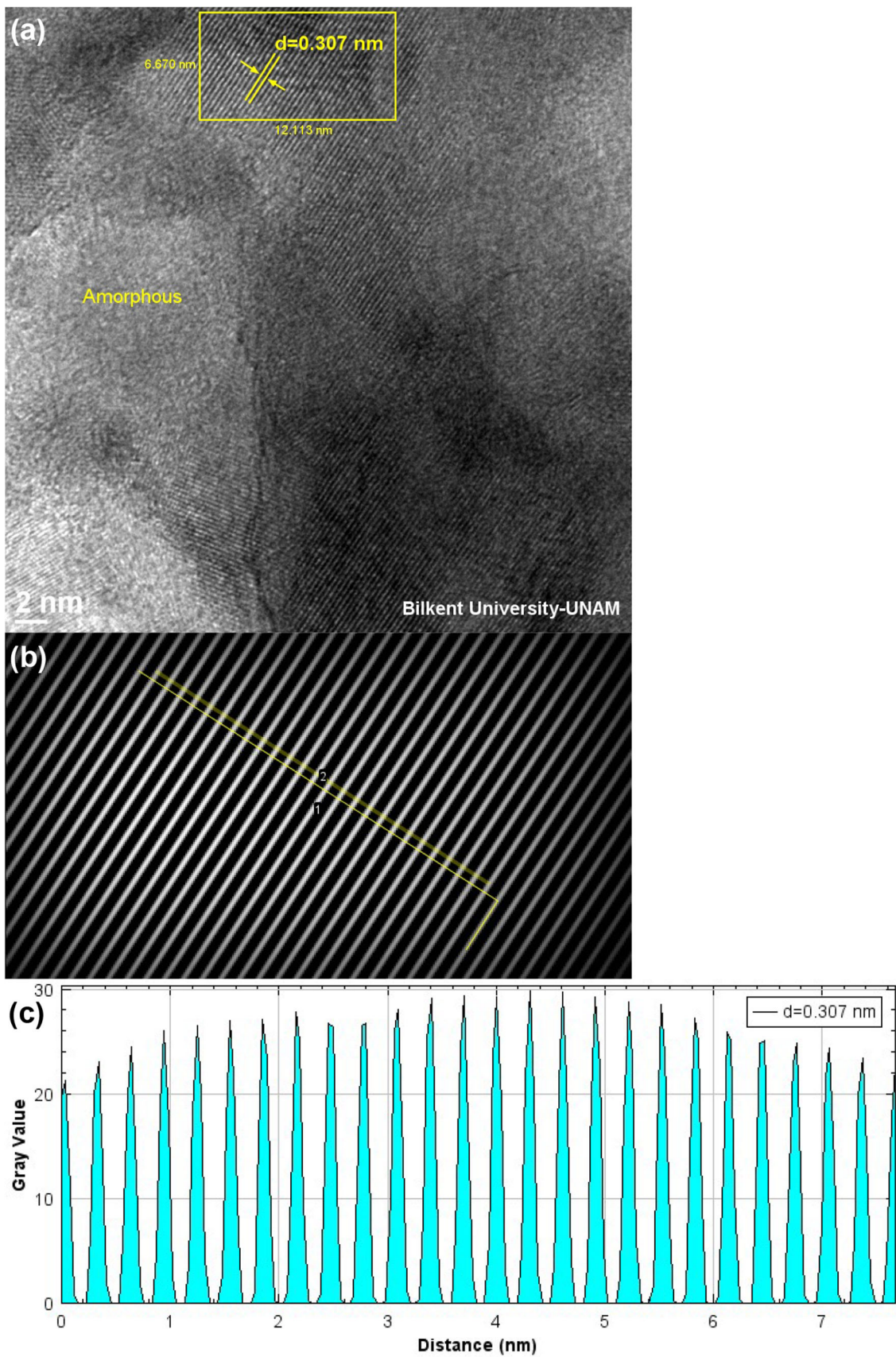


Fig. 8 a HRTEM micrograph, b inverse FFT, and c plot profile of nano-sized amorphous colemanite powder

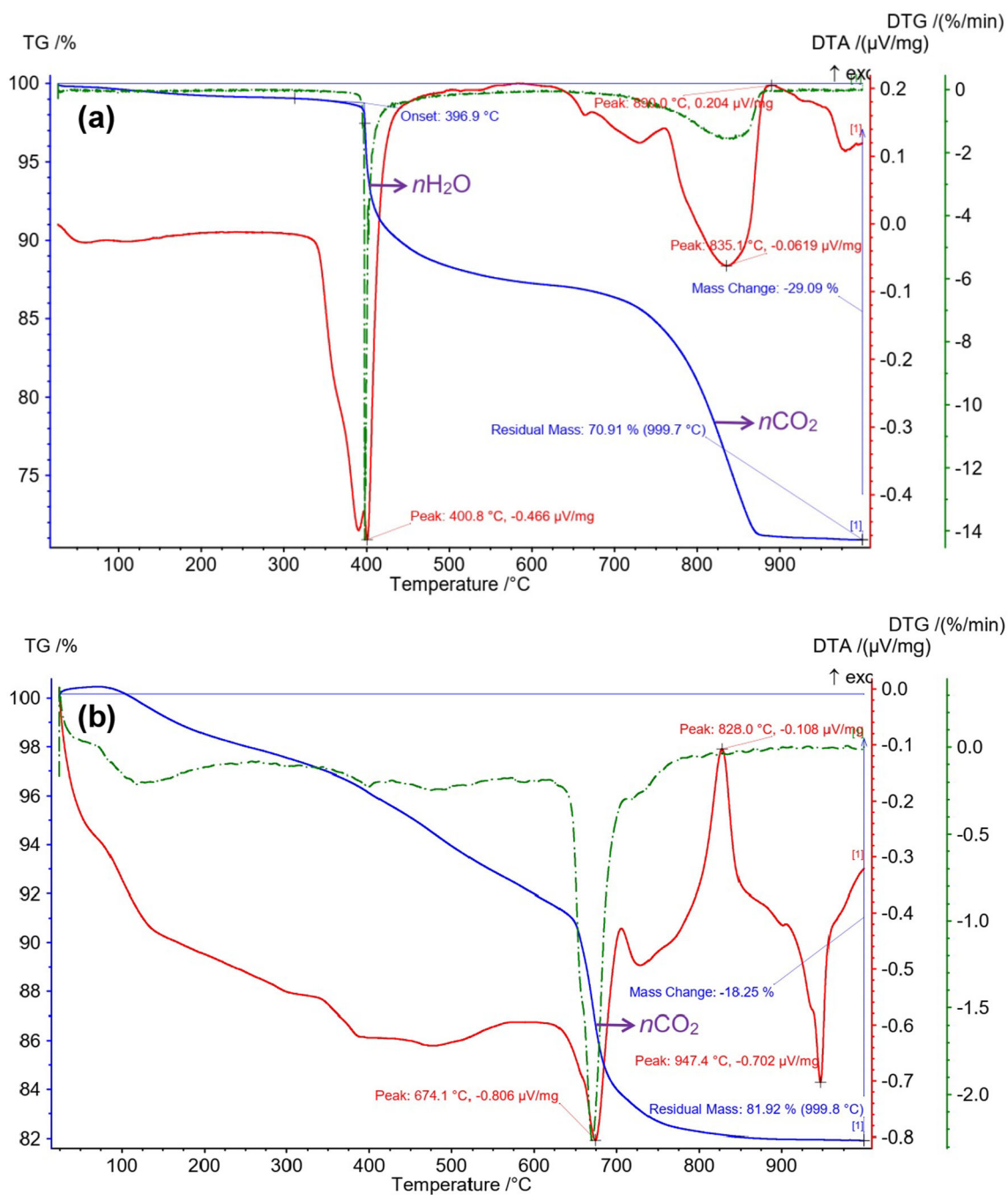
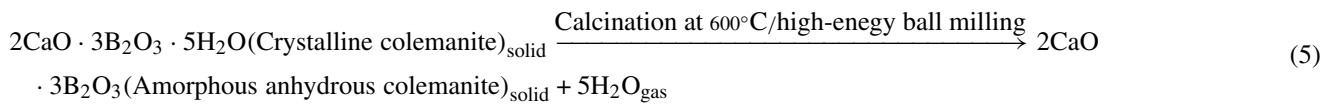


Fig. 9 TGA–DTA curves for **a** raw colemanite mineral and **b** nano-sized amorphous colemanite powder



Lotti et al. [36] published that mortar-ground colemanite mineral possessed a mass loss of 23.0% (22% excluding moisture) on the TG curve at 500 °C, which suggests that the whole of the crystal water being equivalent to 21.8 wt% in the chemical component test was separated from the structure (anhydrous colemanite). On the other hand, in the present study, the mass loss at 500 °C is 12% (11% excluding moisture) for the RC mineral and 6% (4% excluding moisture) for the NAC powder. It is assumed that the less mass loss in the RC mineral (11%) is caused by not only the existence of crystal calcite mineral detected in the XRD analysis as defined by Akpınar et al. [37] (as specified in Fig. 6a, b in the present study, as well), but also factors such as the presence of other impurities, varying B₂O₃ percentage, TGA–DTA/calcination conditions, and the mineral milling process. Additionally, as mentioned above, the difference between the NAC powder and the RC mineral (7%) results from the HEBM process.

In the DTG curve, a small and broad endothermic peak was observed at 120 °C, which emerged from moisture evaporation. It was noticed that the sensitivity of the milled powder to moisture slightly increased. Besides, the largest endothermic peak was described at 674 °C in the DTG curve. This is most probably thought to be owing to the CO₂ release (Eq. (4)). This data, which is in accordance with the DTA data, declined by 161 °C in comparison with the RC mineral (from 835 to 674 °C) and this is very likely due to the HEBM technique. In the DTA curve, endothermic peaks were slighted at 674 °C and 947 °C while a large exothermic peak was found at 828 °C. When compared with the RC mineral, it was deduced that the T_g , T_c , and T_m peaks were different. A similar behavior was observed in previous study [38] within the 625–900 °C interval of the RC mineral milled for 30 min using the HEBM technique, and the peak temperature values were determined to drop. Finally, Lotti et al. [36] declared that the fully anhydrous amorphous colemanite begins to recrystallize at temperatures above 500 °C.

The comment regarding the disappearance of the twin peaks in Fig. 9b can be associated with the EDS explanation in Fig. 5b. It was said that at the end of the milling process, the impurity components increased by 5.4%, 2.3% of which originated from Zr contamination. Hence, it is supposed that the remaining difference of 3.1% stems from the vaporization of the crystal water within the structure of the NAC powder.

In glass and ceramic industries, mineral additives having no crystal H₂O, having no CO₂, being lower characteristic temperatures such as melting, being in an amorphous state and being fine size particles/crystals are important in the point of view of both saving on production costs and reducing environmental pollution. Thus, such properties acquired by the colemanite mineral through the milling process may be a focus of interest for these industries.

4 Conclusion

Raw colemanite (RC) mineral was synthesized via the HEBM technique based on Taguchi design. According to signal-to-noise (S/N) ratio, the sample with the smallest particle size was obtained with the nano-sized amorphous colemanite (NAC) powder. The major findings are drawn as follows:

- In the laser PSD analysis, it was determined that the NAC powder exhibited a non-uniform distribution and had a small peak within the 300–20-nm interval. This indicates that the nanoparticles were successfully obtained.
- It was calculated that the colemanite mineral possessed 71 wt% purity based on mass percent composition for the 36 wt% B₂O₃ value. It was understood that the CaO component supplied by the manufacturer not only belonged to the colemanite mineral, but also to impurity minerals such as CaCO₃.
- In the SEM analysis, it was clearly observed that the particles were agglomerated.
- In the EDS analysis, it was detected that the NAC powder was contaminated with 2.3% Zr by weight from the vial and the balls.
- In the XRD analysis, it was ascertained that calcite and silica minerals in the RC mineral were minor phases, but were present in significant amounts. Additionally, a zirconia peak was described in the NAC powder. The crystal structure almost turned into amorphous and the crystallite size of peak (031) of the colemanite mineral was reduced from 228 to 7.3 nm.
- In the HRTEM micrograph, the Gaussian curve drawn in the histogram was in accordance with the $R^2 = 0.86$ and the average particle size was estimated as 8.29 nm. This success was attributed to the mobility of the balls. The d -spacing value in TEM fringes was calculated as 0.307 nm.
- In the TGA–DTA analysis, a two-step transition occurred within the intervals of 325–500 °C and 700–900 °C. The second of these is an unknown behavior and is thought to originate from the decomposition of the calcite mineral. The complete disappearance of twin peaks for the NAC powder means that the crystal structure turned into amorphous.

Nano-sized amorphous colemanite powder will shed light on engineering studies that will use it as a mineral additive. It is recommended to investigate the effect of this synthesized powder in applications such as concrete, concrete road, asphalt pavement, heat insulation, glass, and ceramics.

Acknowledgements The author would like to express the sincere gratitude to Eti Mining Operations General Directorate for supplying the raw boron mineral, to Dr. T. Kutuk for helping to define optimization of milling parameters, to Prof. A. Canakci for help in using the laser

diffraction particle size analyzer, and to Dr. Y. Demir for help in using the optical microscopes.

Funding Open access funding provided by the Scientific and Technological Research Council of Türkiye (TÜBİTAK).

Declarations

Conflict of interest The author declares that there is no conflict of interest regarding the publication of this manuscript.

Open Access This article is licensed under a Creative Commons Attribution 4.0 International License, which permits use, sharing, adaptation, distribution and reproduction in any medium or format, as long as you give appropriate credit to the original author(s) and the source, provide a link to the Creative Commons licence, and indicate if changes were made. The images or other third party material in this article are included in the article's Creative Commons licence, unless indicated otherwise in a credit line to the material. If material is not included in the article's Creative Commons licence and your intended use is not permitted by statutory regulation or exceeds the permitted use, you will need to obtain permission directly from the copyright holder. To view a copy of this licence, visit <http://creativecommons.org/licenses/by/4.0/>.

References

- Annual Report. Eti Maden Operations General Directorate, Ankara, Turkey (2013)
- Yunlu, K.: Bor bileşikleri, sentez yöntemleri, özellikleri, uygulamaları. BOREN, Ankara, Turkey (2016)
- Kutuk-Sert, T.; Kutuk, S.: Physical and marshall properties of borogypsum used as filler aggregate in asphalt concrete. *J. Mater. Civ. Eng.* **25**, 266–273 (2013). [https://doi.org/10.1061/\(ASCE\)MT.1943-5533.0000580](https://doi.org/10.1061/(ASCE)MT.1943-5533.0000580)
- Kutuk-Sert, T.: Stability analyses of submicron-boron mineral prepared by mechanical milling process in concrete roads. *Constr. Build. Mater.* **121**, 255–264 (2016). <https://doi.org/10.1016/j.conbuildmat.2016.05.156>
- Annual Report. Eti Maden Operations General Directorate, Ankara, Turkey (2019)
- Hosokawa, M.; Nogi, K.; Naito, M.; Yokoyama, T.: Nanoparticle Technology Handbook., Spain (2012)
- Han, W.; Ma, Z.; Liu, S.; Ge, C.; Wang, L.; Zhang, X.: Highly-dispersible boron nitride nanoparticles by spray drying and pyrolysis. *Ceram. Int.* **43**, 10192–10200 (2017). <https://doi.org/10.1016/j.ceramint.2017.05.045>
- Shariatmadar, F.S.; Pakdehi, S.G.: Synthesis and characterization of aviation turbine kerosene nanofuel containing boron nanoparticles. *Appl. Therm. Eng.* **112**, 1195–1204 (2017). <https://doi.org/10.1016/j.applthermaleng.2016.09.015>
- Ding, X.; Huang, Y.; Li, G.; Tang, Y.; Li, X.; Huang, Y.: Phosphorus nanoparticles combined with cubic boron nitride and graphene as stable sodium-ion battery anodes. *Electrochim. Acta* **235**, 150–157 (2017). <https://doi.org/10.1016/j.electacta.2017.03.055>
- Icten, O.; Hosmane, N.S.; Kose, D.A.; Zumreoglu-Karan, B.: Production of magnetic nano-bioconjugates via ball milling of commercial boron powder with biomolecules. *J. Inorg. Gen. Chem.* **642**, 828–832 (2016). <https://doi.org/10.1002/zaac.201600181>
- Yeap, S.P.: Permanent agglomerates in powdered nanoparticles: formation and future prospects. *Powder Technol.* **323**, 51–59 (2018). <https://doi.org/10.1016/j.powtec.2017.09.042>
- Alizadeh, M.; Sharifianjazi, F.; Haghshenasjazi, E.; Aghakhani, M.; Rajabi, L.: Production of nanosized boron oxide powder by high-energy ball milling. *Synth. React. Inorg. Met. Nano-Metal Chem.* **45**, 11–14 (2015). <https://doi.org/10.1080/15533174.2013.797438>
- Waclawska, I.: Thermal behaviour of mechanically amorphized colemanite: I. thermal decomposition of ground colemanite. *J. Therm. Anal.* **48**, 145–154 (1997). <https://doi.org/10.1007/BF01978974>
- Uysal, T.; Mutlu, H.S.; Erdemoğlu, M.: Effects of mechanical activation of colemanite (Ca₂B₆O₁₁·5H₂O) on its thermal transformations. *Int. J. Miner. Process.* **151**, 51–58 (2016). <https://doi.org/10.1016/j.minpro.2016.04.006>
- Kutuk, S.; Kutuk-Sert, T.: An examination of nanoparticle colemanite mineral added warm mix asphalt. *Constr. Build. Mater.* **243**, 118252 (2020). <https://doi.org/10.1016/j.conbuildmat.2020.118252>
- Kutuk, S.: Öğütülmüş nano boyutlu kolemanit mineralinin elementel ve kristal yapı özellikleri. *Erzincan Üniversitesi Fen Bilimleri Enstitüsü Dergisi* **10**, 303–313 (2017)
- Kestelek colemanite product data sheet. Eti Maden Operations General Directorate, Ankara (2014)
- Kutuk, S.; Kutuk-Sert, T.: Effect of PCA on nanosized ulexite material prepared by mechanical milling. *Arab. J. Sci. Eng.* **42**, 4801–4809 (2017). <https://doi.org/10.1007/s13369-017-2643-7>
- Kutuk, S.: Influence of milling parameters on particle size of ulexite material. *Powder Technol.* **301**, 421–428 (2016). <https://doi.org/10.1016/j.powtec.2016.06.020>
- Canakci, A.; Erdemir, F.; Varol, T.; Patir, A.: Determining the effect of process parameters on particle size in mechanical milling using the Taguchi method: measurement and analysis. *Measurement* **46**, 3532–3540 (2013). <https://doi.org/10.1016/j.measurement.2013.06.035>
- Ren, R.; Yang, Z.; Shaw, L.L.: Polymorphic transformation and powder characteristics of TiO₂ during high energy milling. *J. Mater. Sci.* **35**, 6015–6026 (2000). <https://doi.org/10.1023/A:1026751017284>
- Guzzo, P.L.; Marinho de Barros, F.B.; Soares, B.R.; Santos, J.B.: Evaluation of particle size reduction and agglomeration in dry grinding of natural quartz in a planetary ball mill. *Powder Technol.* **368**, 149–159 (2020). <https://doi.org/10.1016/j.powtec.2020.04.052>
- Garg, V.; Mallick, S.S.; Garcia-Trinanes, P.; Berry, R.J.: An investigation into the flowability of fine powders used in pharmaceutical industries. *Powder Technol.* **336**, 375–382 (2018). <https://doi.org/10.1016/J.POWTEC.2018.06.014>
- Helvacı, C.; Öztürk, Y.Y.; Emmermann, A.: Fluorescence survey of Turkish borate minerals: comparative measurements of fluorescence spectra of the most important borate mineral species, Turkey. *Neues Jahrb. für Mineral. Abhandlungen.* **194**, 1–17 (2017). <https://doi.org/10.1127/njma/2016/0016>
- Shin, H.-S.; Lee, B.-K.: Agglomeration parameter, aggregation number, and aggregate porosity. *J. Mater. Sci.* **32**, 4803–4806 (1997). <https://doi.org/10.1023/A:1018691216640>
- Zhang, F.L.; Zhu, M.; Wang, C.Y.: Parameters optimization in the planetary ball milling of nanostructured tungsten carbide/cobalt powder. *Int. J. Refract. Met. Hard Mater.* **26**, 329–333 (2008). <https://doi.org/10.1016/j.ijrmhm.2007.08.005>
- Saghir, M.; Umer, M.A.; Ahmed, A.; Monir, N.B.; Manzoor, U.; Razaq, A.; Xian, L.; Mohammad, K.; Shahid, M.; Park, Y.-K.: Effect of high energy ball milling and low temperature densification of plate-like alumina powder. *Powder Technol.* **383**, 84–92 (2021). <https://doi.org/10.1016/j.powtec.2021.01.026>
- Yildiz, O.: The effect of heat treatment on colemanite processing: A ceramics application. *Powder Technol.* **142**, 7–12 (2004). <https://doi.org/10.1016/j.powtec.2004.03.006>



29. Rajkovic, V.; Romhanji, E.; Mitkov, M.: Characterization of high-energy ball milled prealloyed copper powder containing 2.5 wt% Al. *J. Mater. Sci. Lett.* **21**, 169–173 (2002). <https://doi.org/10.1023/A:1014209618494>
30. Gostariani, R.; Asadabad, M.A.; Paydar, M.H.; Ebrahimi, R.: Morphological and phase evaluation of Al/15 wt% BN nanocomposite synthesized by planetary ball mill and sintering. *Adv. Powder Technol.* **28**, 2232–2238 (2017). <https://doi.org/10.1016/j.apt.2017.06.004>
31. Ghayour, H.; Abdellahi, M.; Bahmanpour, M.: Optimization of the high energy ball-milling: modeling and parametric study. *Powder Technol.* **291**, 7–13 (2016). <https://doi.org/10.1016/J.POWTEC.2015.12.004>
32. Boschetto, A.; Bellusci, M.; La Barbera, A.; Padella, F.; Veniali, F.: Kinematic observations and energy modeling of a Zoz Simoloyer high-energy ball milling device. *Int. J. Adv. Manuf. Technol.* **69**, 2423–2435 (2013). <https://doi.org/10.1007/s00170-013-5201-9>
33. Klimenko, N.N.; Mikhailenko, N.Y.; Delitsin, L.M.; Sigaev, V.N.: Effect of particle size of quartz sand filler on microstructure and strength of alkali-activated slag-based materials. *Arab. J. Sci. Eng.* **46**, 4337–4352 (2021). <https://doi.org/10.1007/S13369-020-04935-3/FIGURES/15>
34. Waclawska, I.: Thermal behaviour of mechanically amorphized colemanite: II. Internal structure reconstitution processes of ground colemanite. *J. Therm. Anal.* **48**, 155–161 (1997). <https://doi.org/10.1007/BF019789755>
35. Gunasekaran, S.; Anbalagan, G.: Spectroscopic study of phase transitions in natural calcite mineral. *Spectrochim. Acta Part A Mol. Biomol. Spectrosc.* **69**, 1246–1251 (2008). <https://doi.org/10.1016/j.saa.2007.06.036>
36. Lotti, P.; Comboni, D.; Gigli, L.; Carlucci, L.; Mossini, E.; Macerata, E.; Mariani, M.; Gatta, G.D.: Thermal stability and high-temperature behavior of the natural borate colemanite: an aggregate in radiation-shielding concretes. *Constr. Build. Mater.* **203**, 679–686 (2019). <https://doi.org/10.1016/j.conbuildmat.2019.01.123>
37. Akpınar, S.; Evcin, A.; Ozdemir, Y.: Effect of calcined colemanite additions on properties of hard porcelain body. *Ceram. Int.* **43**, 8364–8371 (2017). <https://doi.org/10.1016/j.ceramint.2017.03.178>
38. Kutuk, S.; Kutuk-Sert, T.: Nanopartikül kolemanit mineralinin ısı özellikleri ve uygulamada sağlayacağı kazanımlar. *Gümüşhane Üniversitesi Fen Bilimleri Enstitüsü Dergisi* **11**, 198–208 (2020)

